Journal of Power Sources 196 (2011) 9141–9147

Contents lists available at ScienceDirect

Journal of Power Sources

journal homepage: www.elsevier.com/locate/jpowsour

Structure, chemical stability and mixed proton–electron conductivity in $BaZr_{0.9-x}Pr_xGd_{0.1}O_{3-\delta}$

Anna Magrasó[a,*], Carlos Frontera[b], Anette E. Gunnæs[c], Albert Tarancón[d], David Marrero-López[e], Truls Norby[a], Reidar Haugsrud[a]

[a] Department of Chemistry, Centre for Materials Science and Nanotechnology, University of Oslo, FERMiO, Gaustadalleen 21, NO-0349 Oslo, Norway
[b] Institut de Ciència de Materials de Barcelona, ICMAB-CSIC, Campus Universitari de Bellaterra, E-08193 Bellaterra, Spain
[c] Department of Physics, University of Oslo, FERMiO, Gaustadalleen 21, NO-0349 Oslo, Norway
[d] IREC, Catalonia Institute for Energy Research, Department of Advanced Materials for Energy, Jardí de les Dones de Negre 1, Planta 2, Sant Adrià del Besòs, Barcelona, Spain
[e] Deparment of Applied Physics I, University of Málaga, 29071 Málaga, Spain

ARTICLE INFO

Article history:
Received 3 March 2011
Received in revised form 14 April 2011
Accepted 22 June 2011
Available online 18 July 2011

Keywords:
$BaZrO_3$
$BaPrO_3$
Mixed electron–proton conductor
Proton conductor
Perovskite

ABSTRACT

$BaZr_{0.9-x}Pr_xGd_{0.1}O_{3-\delta}$ ($x = 0.3$ and 0.6) was prepared by combustion synthesis and characterised with respect to conductivity and stability in an attempt to combine the desirable properties of the end members. The polycrystalline materials exhibit a cubic or pseudo-cubic structure as determined by X-ray synchrotron radiation and transmission electron microscopy. The chemical stability of the compositions is strongly dependent on the praseodymium content, the materials with more Pr present lower stability. Electron holes dominate the conductivity under oxidising atmospheres in $BaZr_{0.3}Pr_{0.6}Gd_{0.1}O_{3-\delta}$, while $BaZr_{0.6}Pr_{0.3}Gd_{0.1}O_{3-\delta}$ exhibits a mixed electron hole–proton conducting behaviour. Substitution of Zr by Pr in acceptor-doped $BaZrO_3$ decreases the sintering temperature and increases the grain growth rate.

1. Introduction

Perovskite-type oxides (ABO_3) that are dominated by protonic defects at intermediate temperatures are interesting for different technological applications [1–4]. They can for instance be used as electrolytes in proton-conducting solid oxide fuel cells (PC-SOFC) if the proton transference number is close to unity, or in (hydrogen) gas separation membranes and/or electrode components for PC-SOFCs if electrons/electron holes also contribute significantly to the total conductivity.

Acceptor-doped $BaZrO_3$ is among state-of-the-art proton conductors [5] as it exhibits grain interior proton conductivities of the order of 10^{-2} S cm^{-1} at 500 °C combined with excellent chemical stability and mechanical strength. However, it requires very high sintering temperatures (~1700 °C) to obtain dense ceramics, making fabrication troublesome. In addition, the high grain boundary resistance typical of $BaZrO_3$ decreases the overall conductivity, limiting the final performance in high-drain applications. $BaPrO_3$ based materials are other examples of Ba-containing perovskites where protons and oxygen vacancies, as well as electron holes, contribute to the electroneutrality. The overall conductivity of praseodymates is predominated by electron holes [6–10]. These materials are easy to sinter at moderate temperatures [11] and stable under oxidising conditions, but the chemical stability towards reducing gases and/or atmospheres containing CO_2 is limited [6–8,11]. It was shown that Gd-doped $BaPrO_3$ and $BaZrO_3$ form a solid solution [12] and reported that Zr improved the chemical endurance, while increased amounts of Pr seemed to accelerate grain growth and enhanced the sinterability of the zirconate.

Consequently, one may search for compounds within the $BaZrO_3$–$BaPrO_3$ solid solution which combine the desired properties of the end members; on the Pr-rich side a mixed proton–electron hole conductor for PCFC electrodes or hydrogen permeable membranes, and on the Zr-rich side, a proton conductor easier to process and with lower grain boundary resistance than $BaZrO_3$.

In the present work, we mainly focus on the synthesis and characterization of two chosen compositions within the Gd substituted $BaPrO_3$–$BaZrO_3$ solid-solubility range: $BaZr_{0.3}Pr_{0.6}Gd_{0.1}O_{3-\delta}$ (**Pr60**) and $BaZr_{0.6}Pr_{0.3}Gd_{0.1}O_{3-\delta}$ (**Pr30**). Results from the Zr-free material ($BaPr_{0.9}Gd_{0.1}O_{3-\delta}$, **Pr90**, from Ref. [7]) are included for comparison.

A variety of characterization techniques have been applied, including X-ray diffraction (XRD), synchrotron powder diffraction

* Corresponding author. Tel.: +47 22840660; fax: +47 22840651.
E-mail addresses: a.m.sola@smn.uio.no, annamagraso@gmail.com (A. Magrasó).

0378-7753/$ – see front matter © 2011 Elsevier B.V. All rights reserved.
doi:10.1016/j.jpowsour.2011.06.076

(SPD), transmission electron microscopy (TEM), scanning electron microscopy (SEM), and thermogravimetric (TG) analysis. The applicability of these materials as membranes for hydrogen separation, electrodes and electrolytes for PC-SOFCs will be discussed in view of their stability and conductivity.

2. Experimental

2.1. Powder synthesis and sintering

Nanometric powders of $BaZr_{0.3}Pr_{0.6}Gd_{0.1}O_{3-\delta}$ (**Pr60**) and $BaZr_{0.6}Pr_{0.3}Gd_{0.1}O_{3-\delta}$ (**Pr30**) were prepared by dissolving appropriate ratios of Pr_6O_{11}, Gd_2O_3, $ZrONO_3{\cdot}xH_2O$ (all 99.9%, Alfa Aesar, Karlsruhe, Germany) and $BaCO_3$ (99.98%, Sigma Aldrich) in a nitric acid aqueous solution [12,13]. The crystallographic water in the zirconium precursor was determined gravimetrically prior to the synthesis. After the addition of tetra-acidic EDTA, the solution was neutralized with NH_3, dried and then combusted at 700 °C for 5 h. The powders were calcined at 1100 °C for 5 h, pressed into pellets and finally sintered at 1500 °C for 5 h, both steps under air. A pellet of the same composition was placed between the alumina support and the specimen during sintering to prevent reactions with the support.

The morphology and microstructure of the sintered pellets were checked by scanning electron microscopy (SEM) using a Quanta 200 FEG, FEI. The relative density was determined from the mass, sample dimensions, and the theoretical density calculated from lattice cell parameters. Microanalyses were performed in the SEM by Energy Dispersive Spectroscopy (EDS) using a Pegasus 2200 Microcharacterization system from EDAX.

X-ray Diffraction patterns were collected with a PANalytical X'Pert Pro diffractometer, equipped with a Ge(1 1 1) primary monochromator with Cu $K_{\alpha1}$ radiation and the X'Celerator detector. The scans were performed in the 2θ range 10–90° with 0.016° step for 1 h.

2.2. Structural characterization

The average structure was determined from synchrotron powder diffraction (SPD) for **Pr60** and **Pr30**. SPD data were collected using an ultra-high resolution ID31 diffractometer [$\lambda = 0.399979(12)$ Å] of the European Synchrotron Radiation Facility (ESRF, Grenoble) at room temperature. This short wavelength was selected with a double-crystal Si(1 1 1) monochromator to reduce the absorption and calibrated with Si NIST ($a = 5.43094$ Å). Optimum transmission was achieved by enclosing finely ground powder in a spinning borosilicate glass capillary of diameter 0.3 mm. Powder diffraction patterns have been refined by the Rietveld method using FullProf suite of programs [14].

Local structure determination was carried out by selected area diffraction (SAD) in an analytical JEOL 2010F transmission electron microscope with a Field Emission Gun. The TEM specimens were prepared by crushing the materials in ethanol and depositing a droplet on a holey C-grid.

2.3. Thermogravimetric measurements and stability tests

Thermogravimetric (TG) analyses were performed with a Perkin Elmer instrument (Pyris Diamond) on powders fired at 1500 °C in order to study the stability in reducing atmospheres and the hydration/dehydration characteristics. The heating/cooling rate was 10 °C min^{-1} up to 800 °C in all cases, and the atmosphere was ~2% H_2O–5% H_2–Ar. The heating/cooling cycle was repeated in order to check for reproducibility of the measurements.

In addition to these TG tests, the stability of the materials was tested by annealing ~1 g of each composition under wet reducing conditions (~2% H_2O–5% H_2–Ar) at 900 °C for 15 h, followed by room temperature XRD analysis.

2.4. Conductivity

The electrical conductivity of sintered specimens was measured in a ProboStat measurement cell (NorECs, Norway) by the four-point van der Pauw method, with Pt wires as electrodes. The conductivities were corrected for porosity using the empirical first approximation $\sigma = \sigma_{measured}/d_r^2$, where d_r is the relative density [15,16].

Conductivity isobars were measured on cooling from 1000 to ~200 °C in steps of 50–100 °C in wet (~2.5% H_2O) and dry (~3×10^{-5} atm H_2O) oxygen, where the conductivity readings were taken after 30 min of equilibration at every temperature.

3. Results

3.1. Phase formation

The XRD patterns collected at room temperature for **Pr30** after firing at 1100 °C and 1500 °C are displayed in Fig. 1. The patterns do not exhibit traces of simple oxides or carbonates, and mainly show the reflections of a cubic (or pseudo-cubic) perovskite structure. However, the diffraction peaks for the sample calcined at 1100 °C are very asymmetric at low angles, and seemingly split into 2 peaks at higher angles. This does not happen for the specimen sintered at 1500 °C (a similar behaviour is observed for **Pr60**), reflecting that the formation of $BaZr_{0.6}Pr_{0.3}Gd_{0.1}O_{3-\delta}$ is incomplete during calcination at 1100 °C. The broadening and splitting of the peaks may accordingly represent two phases of similar structure but with a slightly different Pr/Zr ratio.

Fig. 2 depicts the XRD patterns for **Pr90**, **Pr60** and **Pr30** after sintering at 1500 °C. Single phase materials with a cubic or pseudo-cubic perovskite structure are apparent. $BaPrO_3$ is reported to exhibit the orthorhombic *Pnma* structure [9,17] while $BaZrO_3$ crystallizes as a primitive $Pm\bar{3}m$ cell [18]. It is clear from the insets of Fig. 2 that the extent of the orthorhombic distortion decreases with increasing Zr content, as expected from the symmetry of $BaZrO_3$. The positions of the main peaks gradually shift towards higher angles with the increase of Zr, and the relative intensities of some of the peaks gradually change as a function of composition, suggesting that they form a solid solution. The variation of the molar cell volume (not shown) due to the substitution of Pr(IV) for Zr(IV) for $BaZr_{0.7-x}Pr_xGd_{0.3}O_{3-\delta}$ [12] followed a linear relationship with

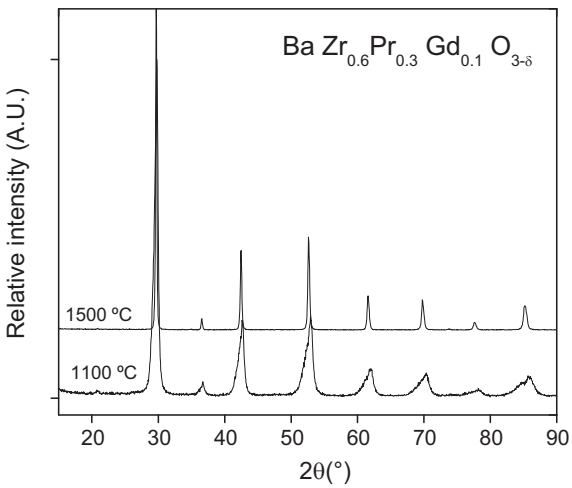

Fig. 1. XRD patterns for $BaZr_{0.6}Pr_{0.3}Gd_{0.1}O_{3-\delta}$ (**Pr30**) after firing at 1100 and 1500 °C.

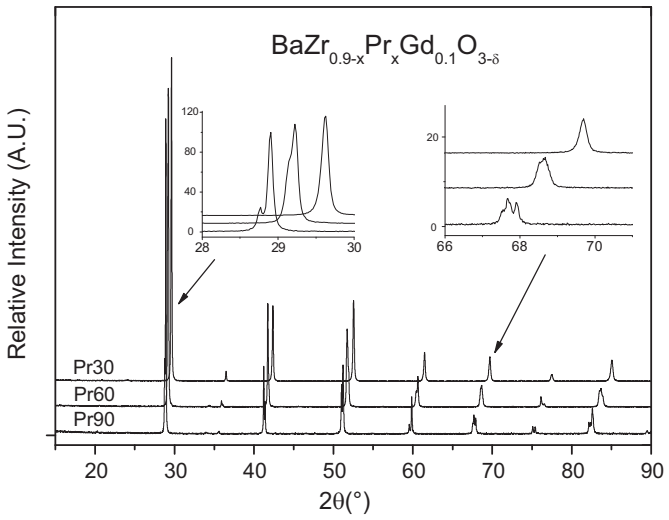

Fig. 2. XRD patterns for **Pr90**, **Pr60** and **Pr30** after sintering at 1500 °C. The inserts show enlarged selected areas of the plot.

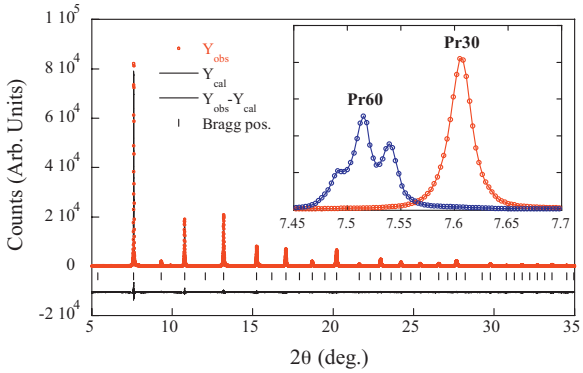

Fig. 3. (Main panel) SPD pattern of **Pr30** refined by the Rietveld method. (Inset) Comparison of the SPD patterns of **Pr30** and **Pr60** at the region where the (1 1 0) peak of the former compound appears.

x. This in accordance with Vegard's law of ideal solid solutions, as the ionic radius of Zr^{4+} ($R = 0.72$ Å) is smaller than that of Pr^{4+} ($R = 0.85$ Å) [19].

The SEM-EDS microanalyses on both **Pr60** and **Pr30** (Table 1) in polished cross-sections gave results similar to those expected from the nominal composition within the uncertainty of the technique.

In order to further elucidate the structure of these materials, higher resolution techniques are required. These will be dealt with in the following section.

3.2. Structure determination

SPD and SAD data show that **Pr30** is a single phase (Figs. 3 and 4). SPD shows that it is possible to index the pattern according to a cubic system, and the Rietveld refinement using a $Pm\bar{3}m$ (no. 221) space group [$a = 4.26503(8)$ Å] rendered good agreement factors ($R_B = 2.58\%$ and $\chi^2 = 3.61$). However, electron diffraction shows extra reflections that are not in accordance with this space group (Fig. 4b). The high angular resolution of the ID31 diffractometer led us to initially discard tetragonal/orthorhombic distortions from the cubic arystotype in this compound. The Rietveld refinement is shown in Fig. 3. Fig. 4a and b shows typical SAD patterns for **Pr30** in the [0 0 1] and [1 1 $\bar{2}$] zone axes. The $(1\,1\,1)_{FCC}$ reflections seen in the [1 1 $\bar{2}$] projection show that the space group $Pm\bar{3}m$ is not correct, and can be indexed as a FCC lattice with a doubling of the unit cell axis initially found by SPD. The extra peaks/reflections in the diffraction data may be ascribed to an ordered arrangement of the cation sublattice, similar to what has been reported by Oikawa et al. [20] for $Ba_3Ca_{1+x}Nb_{2-x}O_{9-\delta}$.

Both SPD and SAD show that the **Pr60** composition is not single-phase. The single diffraction peaks observed in the **Pr30** pattern split into several peaks for the **Pr60** SPD pattern (inset in Fig. 3) and additional reflections are observed by SAD (Fig. 4c). These extra reflections cannot be ascribed to a pseudo-cubic structure. Indexing the SAD pattern (Fig. 4c) using different single cells (orthorhombic or monoclinic) was unsuccessful, and we have, accordingly, only achieved to fit the synchrotron data by using two different crystalline phases: a cubic phase [$a = 4.3045(2)$ Å] and an orthorhombic phase [$a = 6.1053(3)$ Å; $b = 6.1275(3)$ Å; and $c = 8.6281(4)$ Å]. However, this may only be taken as an approximation, since the uncertainty in the composition of each phase prevented us from making an accurate Rietveld refinement of the corresponding structures.

3.3. Sintering

The surface microstructure of the specimens after sintering is shown in Fig. 5. The relative densities of **Pr30** and **Pr60** after sintering at 1500 °C are 89% and 92%, respectively. The grain size also increases significantly from 0.8–3 μm (**Pr30**) to 2–6 μm (**Pr60**) (cf. Fig. 5). For the Zr-free material, **Pr90**, grain sizes of 5–15 μm of diameter and relative densities >96% are obtained for specimens after sintering only at 1400 °C [11]. Consequently, it is clear that the addition of Pr promotes both sintering and grain growth, and thereby that praseodymium can be considered a sintering aid for $BaZrO_3$, as suggested previously [12]. This is beneficial in order to decrease the sintering temperature of the zirconate and facilitate fabrication of components with lower grain boundary resistance. Other studies have shown that substituting Zr for Ce has a similar effect in $BaZrO_3$. For instance, the relative density increases from 65% for $BaZr_{0.9}Y_{0.1}O_{3-\delta}$, 80% for $BaCe_{0.3}Zr_{0.6}Y_{0.1}O_{3-\delta}$ up to 95% for $BaCe_{0.7}Zr_{0.2}Y_{0.1}O_{3-\delta}$ and $BaCe_{0.5}Zr_{0.4}Y_{0.1}O_{3-\delta}$, all sintered

Table 1
Atomic composition of a sintered **Pr60** and **Pr30** specimen determined by EDS.

Element	Spot number					Average ± $2\sigma_{st.dev}$	Nominal
	1	2	3	4	5		
$BaZr_{0.3}Pr_{0.6}Gd_{0.1}O_{3-\delta}$ (**Pr60**)							
Zr	14.6	15.6	16.3	14.5	14.0	15.0 ± 1.9	15
Ba	50.7	49.5	48.9	52.2	50.3	50.3 ± 2.5	50
Pr	29.9	30.4	29.2	28.2	31.0	29.7 ± 2.2	30
Gd	4.6	4.4	5.5	5.0	4.5	4.8 ± 0.9	5
$BaZr_{0.6}Pr_{0.3}Gd_{0.1}O_{3-\delta}$ (**Pr30**)							
Zr	29.3	27.7	28.4	29.4	30.0	29.0 ± 1.8	30
Ba	50.2	52.1	50.9	49.9	48.9	50.4 ± 2.4	50
Pr	15.3	15.6	15.6	15.8	15.9	15.6 ± 0.5	15
Gd	5.0	4.4	4.9	4.7	5.0	4.8 ± 0.5	5

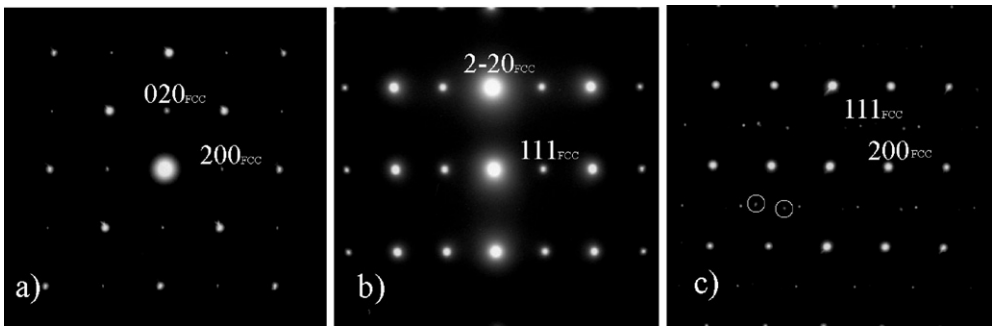

Fig. 4. SAD patterns seen along the (a) [0 0 1], (b) [1 1 $\bar{2}$] projections for **Pr30** and (c) [0 1 $\bar{1}$] projection for **Pr60**. The (1 1 1) reflections cannot be indexed in agreement with $Pm\bar{3}m$, but can be accounted for with a trigonal crystal system with a rhombohedral lattice with the cell parameters $a \sim 6.0$ Å and $\alpha \sim 60°$. Additional reflections, as illustrated with circles in (c), indicate a second phase in **Pr60**.

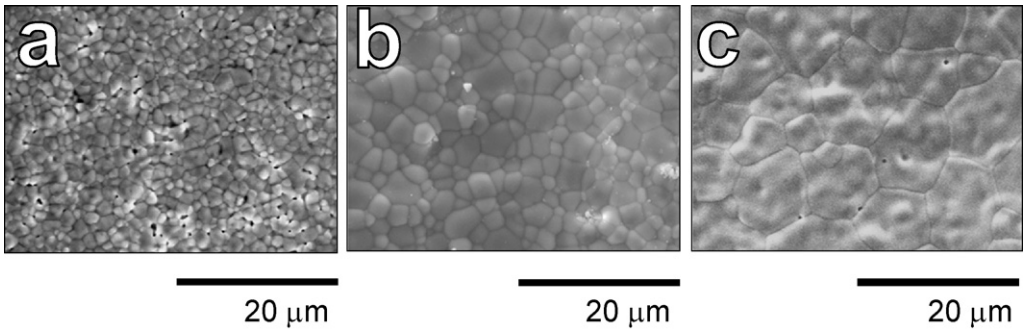

Fig. 5. Representative SEM micrographs of sintered specimens for different compositions: (a) **Pr30** (1500 °C), (b) **Pr60** (1500 °C), and (c) **Pr90** (1400 °C). Notice the marked grain growth with increasing praseodymium content (left to right).

at 1650 °C [21]. Sintering **Pr30** at 1550 °C leads to bodies with ~96% of the relative density and grains of 1–4 μm in diameter [22]. These results suggest that praseodymium is more effective than cerium to increase the sinterability of barium zirconates.

3.4. Thermal analysis and stability

Fig. 6 shows the relative weight change in the TG curves upon cooling under wet reducing conditions (5% H_2–Ar) for **Pr30** (a) and **Pr60** (b). **Pr30** behaves as expected for a material that dissolves protons, i.e. the weight increases on cooling without any anomalous behaviour associated to phase instability. The weight gain corresponds to the reaction between oxygen vacancies and water to form protons:

$$H_2O(g) + v_O^{\bullet\bullet} + O_O^x = 2OH_O^{\bullet} \quad (1)$$

The **Pr30** composition exhibits stable behaviour with reproducible TG curves (cf. Fig. 6a) and no signs of decomposition in the XRD pattern after the treatment in wet 5% H_2–Ar (Fig. 7a). The (pseudo)cubic lattice parameter determined by XRD analyses was 4.266(1) Å after sintering in air and increased to 4.286(1) Å after the thermal treatment in wet atmospheres, in accordance with an expansion of the unit cell due to incorporation of water (Eq. (1)). It should be mentioned that well sintered specimens become brittle after long-term exposure under wet reducing conditions. Although XRD does not reveal formation of additional phases, the intensity of the peaks is lower and broader, which indicates amorphization of the samples. The change in volume corresponding to the RT analogue shows an expansion of the cell volume of ~1.3%, which is in principle an expansion that the structure could tolerate. A possible explanation may be a partial (or total) reduction of Pr(IV) to Pr(III) taking place at high temperatures together with the hydration process, and the perovskite structure may collapse

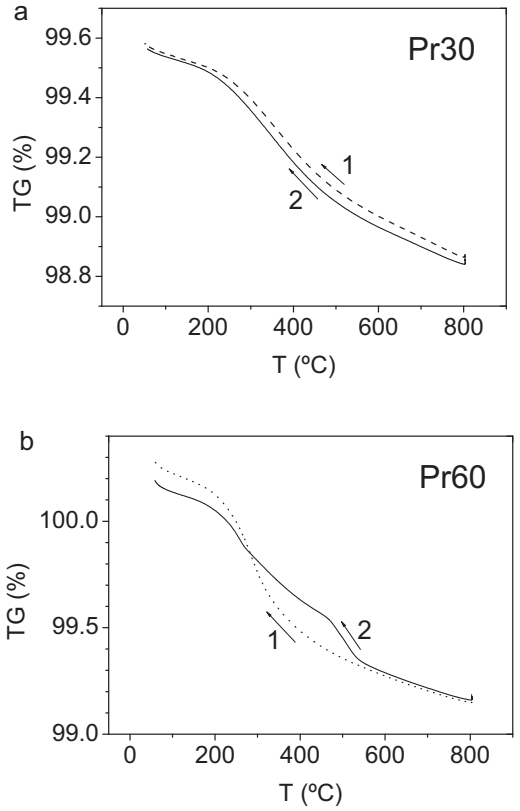

Fig. 6. Thermogravimetric curves under ~2% H_2O–5% H_2/Ar for (a) **Pr30** and (b) **Pr60** during different thermal cycles.

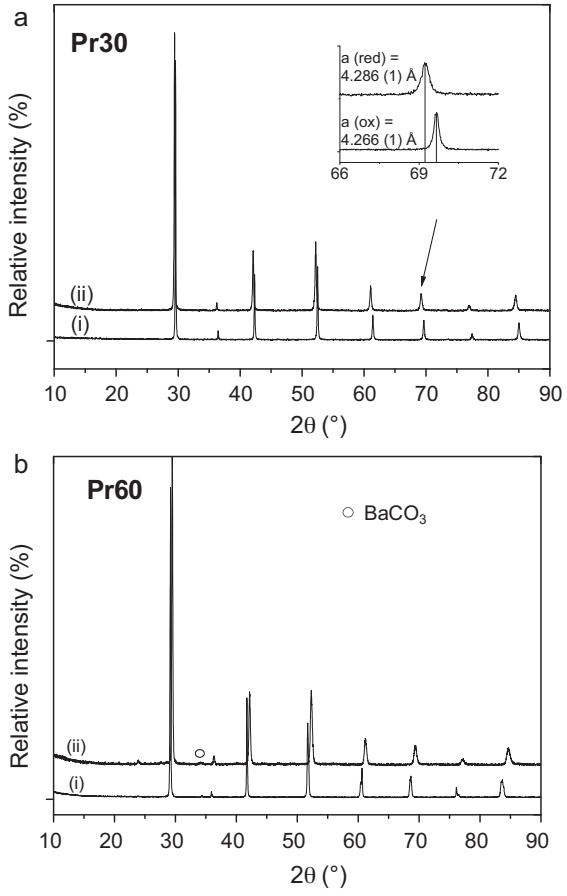

Fig. 7. XRD patterns before (i) and after (ii) a thermal treatment at 900 °C in ~2% H_2O–5% H_2/Ar for (a) **Pr30** and (b) **Pr60**.

during those reactions. Partial decomposition beyond what can be detected by XRD or SEM cannot be excluded either.

The TG curves for **Pr60** (Fig. 6b) are on the other hand not reproducible after different thermal cycles. This shows, as confirmed by XRD, that other parallel reactions are taking place due to the higher praseodymium content, and that this composition is more vulnerable to reduction than **Pr30**. The XRD pattern for **Pr60** after the treatment in wet 5% H_2–Ar (Fig. 7b) does not show reduced compounds, such as $Ba(Gd,Pr)_2O_4$ as reported for **Pr90** after a similar treatment [11,12], but the peaks exhibit lower intensity and formation of small quantities of $BaCO_3$, i.e. less evidence of decomposition. A refinement of the pseudo-cubic lattice parameter for **Pr60** using the Le Bail routine leads to $a = 4.316(2)$ Å after sintering, and decreases to 4.281(1) Å after the reduction process.

3.5. Conductivity

Fig. 8 presents the temperature dependence of the overall DC conductivity for $BaZr_{0.9-x}Pr_xGd_{0.1}O_{3-\delta}$ ($x = 0$, 0.3 and 0.6) in dry and wet O_2. The conductivity decreases and the apparent activation energy increases with increasing content of Zr. This is, as a first approximation, in accordance with an increasing dominance of protons over electron holes in the materials with more Zr. Also, the effect of the water vapour pressure shows a behaviour that is in line with an increasing amount of protons with increasing Zr, as explained in detail below.

For the material without Zr (**Pr90**), there was no measurable proton conductivity, and electron holes dominated both conductivity- and concentration-wise [7]. The fact that the conductivity decreases slightly in the presence of water vapor, indicates

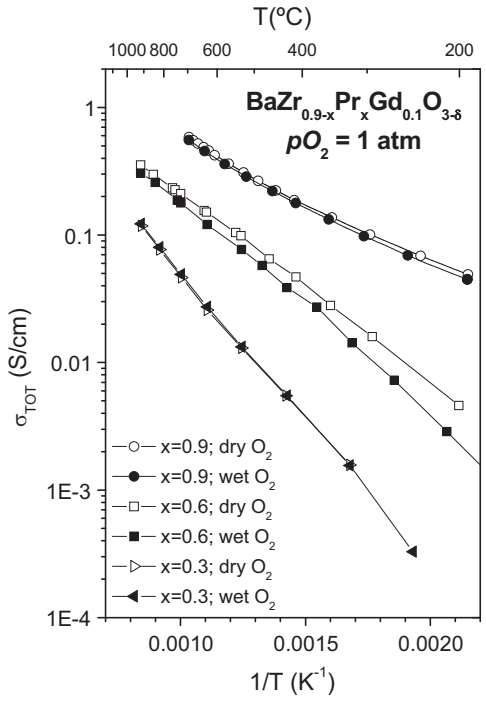

Fig. 8. Comparison of the total conductivity as a function of the inverse temperature for **Pr90**, **Pr60**, and **Pr30** under dry and wet O_2.

a small but significant dissolution of protons suppressing the concentration of the more mobile electron holes [7]:

$$\frac{1}{2}H_2O(g) + h^{\bullet} + O_O^x = OH_O^{\bullet} + \frac{1}{4}O_2(g) \quad (2)$$

Pr60 shows as expected a more prominent effect of water on the conductivity, since higher Zr contents should lead to an increased concentration of protons. However, electron holes are still the dominating charge carriers in O_2 and the presence of water still decreases the overall conductivity according to the reaction in Eq. (2).

The material with the highest Zr content of this study (**Pr30**) behaves differently: there is only a small effect of water on the total conductivity under O_2 and it is not possible to conclude which charge-carriers are dominating with this measurement only. Determination of partial conductivities has been performed using the EMF method under activity gradients in a complementary study [22] and revealed that the material is a mixed electron hole–proton conductor. **Pr30** presents appreciable proton conductivity under wet conditions, of the order of $\sim 10^{-4}$ S cm^{-1} at 500 °C and $\sim 10^{-3}$ S cm^{-1} at 900 °C. Both the proton transport number and the isotope effect were determined to be relatively temperature independent between 900 and 500 °C [22]. This may imply that the combination of the temperature dependence of the migration of holes, migration of protons and the temperature dependence of the reaction in Eq. (2) is such that, circumstantially, it results in small differences in overall conductivity between wet and dry O_2.

4. Discussion

Acceptor-doped $Ba(Pr,Zr)O_3$ materials present several interesting properties from both a fundamental and application point of view. They are electron, mixed electron–proton, or pure proton conductors, depending on the specific composition. **Pr60** has a relatively high conductivity (0.1 S cm^{-1} at 500 °C, in O_2), mainly from electron holes, and is chemically more stable than **Pr90**, which presents even higher conductivities (0.3 S cm^{-1} at 500 °C, in

O_2). Protons contribute significantly to the electroneutrality in wet atmospheres for **Pr90**, but proton conductivity was barely measurable due to the dominance of the highly mobile electron holes. **Pr60** should exhibit higher proton conductivity and may have interesting properties to be used as a cathode component in PC-SOFCs. Despite its relatively high conductivity, it cannot be used for gas separation membrane applications due to its low chemical stability under wet reducing conditions. The stability issues found for **Pr60** are probably due to the relatively high Pr content, rather than its dual phase nature. SEM micrographs from the back-scattered electron detector did not show any evidence of formation of two separate phases, and neither did EDS microanalysis. Consequently, the two compositions must be similar and are only detectable using high-resolution techniques.

Pr30 is chemically more stable, was analyzed in more detail, and will be compared to available relevant literature. This and other studies [22] show that **Pr30** is a mixed ionic-electronic conductor. The protonic conductivity under wet conditions is $\sim 10^{-3}$ S cm^{-1} and $\sim 10^{-4}$ S cm^{-1} at 900 and 500 °C, respectively, while the p-type electronic conductivity is ~0.05 and ~0.004 S cm^{-1} in wet O_2 for the same temperatures [22]. The protonic conductivity of this material is about one order of magnitude smaller than that of $BaZr_{0.9}Y_{0.1}O_{3-\delta}$. Acceptor-doped $BaPrO_3$ is dominated by electron hole conductivity, mainly fixed by the doping concentration and not affected by the type of doping (Y or Gd) [9]. On the other hand, Kreuer [5] reported that protons in Y-doped $BaZrO_3$ are more mobile than in Gd-doped $BaZrO_3$. Therefore, a lower protonic conductivity for the **Pr30** (Gd-doped) compared to $BaZr_{0.9}Y_{0.1}O_{3-\delta}$ is within expectations due to the different dopant type.

In addition to our previous studies on $BaZr_xPr_{0.7-x}Gd_{0.3}O_{3-\delta}$ [12], there have been some efforts to stabilize $BaPrO_3$ by partially replacing Pr by Zr [23–25]. However, none of them report detailed structural or stability studies, and some of the conductivity results, in our opinion, may reflect formation of secondary phases when relatively high praseodymium contents are used, in particular, under reducing conditions. A more recent report [26] has dealt with the structure and stability of $Ba(Pr_{1-x}Zr_x)_{1-y}Y_yO_{3-\delta}$, but no conductivity characterization was reported.

From an application point of view, there is in general a growing interest to find materials that present mixed electron–proton conductivities with applications as either cathode for PC-SOFCs or membranes for hydrogen separation. There is a lack of materials that combine high mixed conductivity with sufficient chemical stability. One could possibly use **Pr30** as cathode material, since the chemical stability is good under oxidising conditions, and the protonic conductivity falls within other state-of-the-art mixed conductors. However, the electronic conductivity of this material may be insufficient to act as current collector and it must then be consequently combined with a ceramic electronic conductor in a cer–cer composite. This may be useful since current collectors used in classical SOFCs (mainly lanthanum cobaltites, ferrites, manganites) have very unfavourable hydration thermodynamics and expectedly low partial protonic conductivity [27]. **Pr30** presents good mixed proton–electron hole conductivities and stability under oxidizing conditions. As a membrane material for hydrogen separation, one should compare the ambipolar proton–electron conductivity under reducing conditions at relatively high temperatures, and compare it with state-of-the-art materials, such as Yb-doped $SrCeO_3$ [28,29]. One may expect n-type conductivity to be relatively high in this material due to the reducibility of Pr, but the composition with 30% Pr is not sufficiently long-term stable under reducing conditions and can hardly be used for hydrogen separation. We may suggest that replacing more Pr by Zr should overcome this problem, although that will lower the electronic conductivity, depending on the extent of substitution. The choice of dopant may also be important, and composition optimisation is needed to further assess this issue.

A remarkable result of this report is that praseodymium substitution for zirconium improves the sinterability of $BaZrO_3$. Others have used ZnO [30,31], NiO [32], Co and Ni [33] to improve densification and grain growth via the formation of intermediate phases, e.g. BaY_2NiO_5. Composition optimisation within a $BaCeO_3$–$BaZrO_3$ solid solution has also been sought in literature [34,35], but it seems that Pr is more effective than Ce to increase the sinterability, and we have also demonstrated an increased grain growth rate by addition of Pr to $BaZrO_3$. If a small amount of Pr is used, the p-type conductivity remains modest, the chemical stability retained, the sintering temperature reduced and the average grain size increased, which in turn will decrease the resistance stemming from the resistive grain boundaries of $BaZrO_3$. Reducing the sintering temperature of barium zirconate is also beneficial not only to facilitate its fabrication, but also to avoid Ba losses reported, for instance, in $BaZrO_3$ [36] and $BaCeO_3$ [37]. A recent publication by Fabbri et al. [38] demonstrates that $BaZr_{0.7}Pr_{0.1}Y_{0.2}O_{3-\delta}$ is easier to obtain dense compared to Y-doped $BaZrO_3$, and can be used as electrolyte in a PC-SOFC, with open circuit voltages ~97% of the theoretical at 600 °C. This means that electronic conductivity is minor and that proton conductivity is dominant for that composition at that temperature. In addition, the chemical stability was reported to be good.

From a fundamental point of view, it is interesting to investigate whether there is an effect on the grain boundary specific conductivity in $BaZrO_3$ when zirconium is sought replaced by Pr. It has been reported that the specific grain interior and grain boundary conductivities in $BaZr_{0.9}Y_{0.1}O_{3-\delta}$ are dominated by ions and an additional n-type electronic contribution for the grain boundary conductivity under reducing conditions [39]. They reported the existence of a positively charged grain boundary core with depletion of positive defects and accumulation of negatively charged defects in the adjacent space-charge layers. One may expect that increasing the concentration of electronic defects (e.g. electrons, Pr'_{pr}) could facilitate the accumulation of negative species in the space-charge layer. This could lead to an apparent improvement in the grain boundary conductivity under reducing conditions in $BaZrO_3$. This will be treated in a separate contribution [22].

5. Conclusions

The present study has demonstrated that the properties of $BaZr_{0.9-x}Pr_xGd_{0.1}O_{3-\delta}$ can be tailored by varying Pr content. By lowering the Pr content, an increase of the chemical stability and share of proton conductivity is encountered. More Pr, on the other hand, results in an enhancement of the sinterability and electronic p-type (hole) conductivity.

Praseodymium may be used to replace zirconium in $BaZrO_3$ to decrease the sintering temperature and enhance grain growth, which are two important key issues to facilitate fabrication of electrolytes based on this material, and to decrease the resistive contribution of the grain boundaries.

Acknowledgements

Authors would like to acknowledge financial support from the Nanomat NanoPCFC (182090/510) project of the Research Council of Norway (RCN).

References

[1] K.-D. Kreuer, Chem. Mater. 8 (1996) 610–641.
[2] H. Iwahara, H. Uchida, K. Ono, K. Ogaki, J. Electrochem. Soc. 135 (1988) 529–533.
[3] T. Norby, Solid State Ionics 125 (1999) 1–11.
[4] N. Bonanos, Solid State Ionics 53–56 (1992) 967–974.
[5] K.-D. Kreuer, Annu. Rev. Res. 33 (2003) 333–359.

[6] K.A. Furøy, R. Haugsrud, M. Hänsel, A. Magrasó, T. Norby, Solid State Ionics 178 (7–10) (2007) 461–467.
[7] A. Magrasó, R. Haugsrud, M. Segarra, T. Norby, J. Electroceram. 23 (1) (2009) 80–88.
[8] V.P. Gorelov, B.L. Kuzin, V.B. Balakireva, N.V. Sharova, G.K. Vdovin, S.M. Beresnev, Y.U.N. Kleshchev, V.P. Brusentsov, Russ. J. Electrochem. 37 (**5**) (2001) 505–511.
[9] C.S. Knee, A. Magrasó, T. Norby, R.I. Smith, J. Mater. Chem. 19 (2009) 3238–3247.
[10] S. Mimuro, S. Shibako, Y. Oyama, K. Kobayashi, T. Higuchi, S. Shin, S. Yamaguchi, Solid State Ionics 178 (2007) 641–647.
[11] A. Magrasó, F. Espiell, M. Segarra, J.T.S. Irvine, J. Power Sources 169 (2007) 53–58.
[12] A. Magrasó, X. Solans, J.T.S. Irvine, M. Segarra, Ceram. Int. 35 (2009) 1819–1827.
[13] A. Magrasó, A. Calleja, X.G. Capdevila, F. Espiell, Solid State Ionics 166 (3–4) (2004) 359–364.
[14] J. Rodríguez-Carvajal, Physica B 192 (1993) 55.
[15] M. Zahid, I. Arul Raj, F. Tietz, D. Stöver, Solid State Sci. 9 (2007) 706.
[16] S. Marion, A.I. Becerro, T. Norby, Ionics 5 (1999) 385–392.
[17] A.J. Jacobson, B.C. Tofield, B.E.F. Fender, Acta Crystallogr. B 28 (1972) 956.
[18] H.E. Swanson, N.Y. Gilfrich, G.M. Ugrinic, Natl. Bur. Std. (U.S.) Circ. 539 (1955) 75.
[19] R.D. Shannon, Acta Cryst A 32 (1976) 751.
[20] K. Oikawa, T. Kamiyama, S. Ikeda, T. Shishido, S. Yamaguchi, Solid State Ionics 154–155 (2002) 641–646.
[21] Z. Zhong, Solid State Ionics 178 (2007) 213–220.
[22] A. Magrasó, Presentation at the Electroceramics XII conference (2010), Trondheim (Norway); submitted for publication.
[23] C. Zuo, Doping and defect structure of mixed-conducting ceramics for gas separation, PhD thesis, Georgia Institute of Technology, USA, 2006.
[24] B. Merinov, A. van Duin, S.M. Haile, W.A. Goddard III, Semi-Annual Technical Progress Report, 2004.
[25] U. Balachandran, T.H. Lee, S. Wang, C. Zuo, S.E. Dorris, 20th Annual International Pittsburgh Coal Conference, 2003.
[26] I. Antunes, G.C. Mather, J.R. Frade, J. Gracio, D.P. Fagg, J. Solid State Chem. 183 (12) (2010) 2826–2834.
[27] T. Norby, Perovskite Oxide for Solid Oxide Fuel Cells, Fuel Cell Hydrogen Energy, 2009, ISBN 978-0-387-77707-8, pp. 217–241.
[28] H. Iwahara, Solid State Ionics 86–88 (1996) 9–15.
[29] S. Hamakawa, T. Hibino, H. Iwahara, J. Electrochem. Soc. 14 (1994) 1720.
[30] S. Tao, J.T.S. Irvine, J. Solid State Chem. 180 (12) (2007) 3493–3503.
[31] S.W. Tao, J.T.S. Irvine, Adv. Mater. 18 (12) (2006) 1581–1584.
[32] J. Tong, D. Clark, M. Hoban, R. O'Hayre, Solid State Ionics 181 (11–12) (2010) 496–503.
[33] S. Ricote, N. Bonanos, Solid State Ionics 181 (15–16) (2010) 694–700.
[34] K.H. Ryu, S.M. Haile, Solid State Ionics 125 (1999) 355.
[35] K. Katahira, Y. Kohchi, T. Shimura, H. Iwahara, Solid State Ionics 138 (2000) 91.
[36] S.M. Haile, G. Staneff, K.H. Ryu, J. Mater. Sci. 36 (2001) 1149.
[37] D. Hirabayashi, A. Tomita, S. Teranishi, T. Hibino, M. Sano, Solid State Ionics 176 (9–10) (2005) 881–887.
[38] E. Fabbri, L. Bi, H. Tanaka, D. Pergolesi, E. Traversa, Adv. Funct. Mater. 21 (2011) 158–166.
[39] C. Kjølseth, H. Fjeld, Ø. Prytz, P.I. Dahl, C. Estournès, R. Haugsrud, T. Norby, Solid State Ionics 181 (5–7) (2010) 268–275.